Analysis of the length scale characterized by the yield stress fluids porosimetry method for consolidated media: comparison with pore network models and mercury intrusion porosimetry

Antonio Rodríguez Castro[1] · Azita Ahmadi-Sénichault[1] · Abdelaziz Omari[2]

Abstract

Substantial progress has been recently achieved in the development of a clean alternative to mercury intrusion porosimetry (MIP) based on single-phase flow measurements in porous samples using yield stress fluids. However, no study to date has examined the scale of the pore length actually provided by the yield stress fluids porosimetry method (YSM) in consolidated porous media. Indeed, while the results of YSM were compared to those provided by MIP in the past, the relationships between the characterized pore size distribution (PSD) and the actual pore geometry have still not been addressed for this type of porous media. This issue is of special interest to geoscientists involved in seeking relevant information from core characterization operations. With this aim in mind, the objective of the present paper is to evaluate the agreement between the PSDs characterized by YSM, the pore-opening size distributions provided by MIP tests, and the pore-throat and pore-body size distributions obtained from X-ray computed microtomography. For this purpose, a set of artificial and natural porous samples with permeability values extending over two magnitudes were characterized by using both YSM and MIP laboratory tests. Then, the results were matched to the model pore geometries extracted from digital images of the real microstructure. This analysis led to the main conclusion that YSM can be reliably used as an adequate substitute for MIP in the case of the investigated consolidated media, given the general agreement observed between these methods.

Introduction

Numerous aquifers worldwide are comprised of consolidated sedimentary strata (Morris et al. 2003)—for example, sandstone and limestone formations store water even in semi-arid and dry regions, and many coastal calcareous formations act as local highly permeable aquifers providing water for cities and irrigation. Other important consolidated aquifers are the basaltic lavas from which prolific springs may stem and the consolidated crystalline basement rocks (Miller 1999; Aizebeokhai and Oyeyemi 2018). Water-bearing rocks can be contaminated by a range of dissolved and immiscible pollutants released by industrial, agricultural or human fecal sources. In these situations, a primary task consists of determining the rate at which contaminants will reach the groundwater and how fast they will migrate to water intake points (Ball et al. 1990; Hancock et al. 2005).

Hydraulic conductivity of idealized cylindrical pores scales quadratically with respect to pore diameter; therefore, the transport of pollutants in aquifers is considerably influenced by the distribution of pore sizes, and, more specifically, by the pore-throat size distribution (TSD) (Bloomfield et al. 2001). The invasion of nonwetting immiscible phases following a spill, e.g., chlorinated hydrocarbon and other dense nonaqueous phase liquids (DNAPLs), is also known to depend on pore-throat sizes (Kueper et al. 1989), as does the amount

✉ Antonio Rodríguez Castro
antonio.rodriguezdecastro@ensam.eu

[1] Present address: I2M, Arts et Métiers Institute of Technology, CNRS, Esplanade des Arts et Métiers, 33405 Talence Cedex, France

[2] I2M, Bordeaux-INP, CNRS, Esplanade des Arts et Métiers, 33405 Talence Cedex, France

and scattering of residual ganglia in the contaminant phase after the drainage step in soil remediation processes. Apart from this, the dimensions of the pore throats also play a significant role in the retention of microbiota, whose sizes typically range from 1 to 10 μm (Harvey and Garabedian 1991; Bloomfield et al. 2001). Consequently, knowledge of pore-throat size distribution is essential when dealing with the study of transport of pollutants and microorganisms in saturated subterranean porous media.

Seminal contributions to the development of a porosimetry method based on the injection of complex fluids have been made by several researchers, as summarized in Table 1. These contributions led to the development of the 'yield stress' fluids porosimetry method (YSM; Rodríguez de Castro et al. 2014), which consists of determining the pore-size distribution (PSD) of a porous medium from the experimental flow rate vs. pressure gradient measurements obtained during the flow of a yield stress fluid. Indeed, a yield stress fluid only flows through a certain number of pores depending on the value of the applied pressure gradient (the fluid is stagnant in more and more pores as the pressure gradient is decreased).

Previous YSM studies on consolidated porous media (Rodríguez de Castro et al. 2018) exclusively focused on the evaluation of the accuracy of the PSDs provided by YSM through comparison with the well-established mercury intrusion porosimetry (MIP) technique. Nevertheless, the choice of MIP as "the reference porosimetry method" is not without controversy. Although MIP has been widely used in the past to characterize consolidated water-bearing rocks (Ball et al. 1990; Bloomfield et al. 2001; Nabawy et al. 2009; Jiao et al. 2020) due to the wide range of pore sizes that can be measured and the relatively short duration of the tests, this method causes serious concerns. First, mercury is a toxic fluid, so the industry is trying to phase out MIP because of the health and safety issues. Moreover, the use of MIP as golden standard is not always advisable due to the risk of fracturing the original pore network (Li et al. 2018a, b), the indiscriminate filling of large and small pores downstream of the opening constrictions (Diamond 2000) and the contamination of the samples with mercury. Also, in the previous work (Rodríguez de Castro et al. 2018), the comparison was undetailed, as the elusive PSD provided by YSM blurred the distinction between pore-throat size and pore-body size because of the lack of analysis of the characterized length scale. Such a distinction is particularly important in straining processes for predicting colloid transport and retention (Bradford et al. 2009; Mirabolghasemi et al. 2015). Indeed, straining occurs when particle sizes are smaller than pore throat diameters, inducing plugging phenomena due to particle accumulation and a loss of fluid injectivity. Hence, a blurred PSD is not enough, and the throat size distribution is required for making good predictions.

As an alternative to MIP, the three-dimensional (3D) microcomputed tomography scan approach provides a direct description of the pore space (Peksa et al. 2015; Feng et al. 2020), in spite of its limitations in terms of spatial resolution (~1 μm), the costly equipment and the complexity of the post-treatment algorithms performed on the reconstructed image. Three-dimensional microtomography can be used to characterize both the connected and the isolated pores, while MIP and YSM can only measure the connected pores through which the injected fluid can flow. As reviewed by Blunt et al. (2003) and Xiong et al. (2016), the distribution of sizes of the pore bodies and the pore throats, as well as their connectivity, can be extracted by means of pore network modelling from digital images of the investigated media. Recent research suggested that, through this method, the PSDs obtained by YSM are related to the size of pore constrictions in which most pressure drop is produced. However, these studies were limited to experimental results in unconsolidated porous media (Rodríguez de Castro et al. 2019) and numerical simulations of yield stress fluids flow through two-dimensional (2D) porous media (Rodríguez de Castro et al. 2020a).

For the reasons already presented, previous research can only be considered as a first-order step towards meeting the industry requirements of a robust porosimetry technique. The overall goal of the present work is to go further by decoding the physical meaning of the pore dimensions characterized by YSM in the case of consolidated porous media. In order to achieve this objective, state-of-the-art pore networks will be extracted from digital images of three widely investigated consolidated porous media obtained by microtomography. At the same time, a set of YSM and MIP tests will be performed on samples of such porous media. By doing so, the closeness of the PSDs determined by YSM to the throat and body size distributions provided by X-ray computed 3D microtomography and to the pore-opening size distribution provided by MIP will be assessed and discussed. For the first time, the results of YSM tests on consolidated materials (natural and artificial media) will be compared to the dimensions characterized by these two well-established techniques, demonstrating the relevance of the method as an alternative to the potentially toxic MIP.

YSM porosimetry method: PSD calculation algorithm

The PSD calculation algorithm used in YSM was described in detail in previous works (Rodríguez de Castro et al. 2014, 2016). Consequently, only the key stages will be summarized in the following paragraphs.

The rheological behaviour of the yield stress fluids used in YSM, assuming simple shear and steady-state conditions, is described by the Hershel-Bulkley model. This empirical law

Table 1 Literature review of the contributions to the development of a porosimetry method based on the injection of complex fluids

Research reference	Summary
Ambari et al. (1990)	Theoretical basis of a porosimetry method based on the injection of yield stress fluids. They showed that the PSD of a bundle of straight circular capillaries can be derived from $(Q, \nabla P)$ measurements during the injection of a Bingham fluid, with Q being the total flow rate through the analyzed porous sample and ∇P being the average pressure gradient
Chaplain et al. (1992)	Extension to a bundle of randomly oriented capillaries
Oukhlef (2011) and Oukhlef et al. (2014)	Extension to Casson and Herschel-Bulkley fluids. Analytical inversion of numerically generated $(Q, \nabla P)$ data by computing the partial derivatives of a polynomial regression of the data. The inversion was highly sensitive to experimental uncertainty and provided noisy results in the small pore-size region
Malvault (2013)	Calculation of the PSDs of model porous media from laboratory flow experiments using yield stress fluids. Alternative numerical inversion including polynomial filtering. The results depended on the order of the polynomial filtering
Rodríguez de Castro (2014) and Rodríguez de Castro et al. (2014)	Filtering-free inversion algorithm adapted to experimental data: the YSM method. Selection and characterization of concentrated xanthan gum solutions as yield stress fluid for laboratory tests. Experimental characterization of artificial consolidated porous media using YSM. The characterized length scale was not analyzed
Rodríguez de Castro et al. (2016)	Use of YSM to characterize a set of natural and artificial consolidated porous media. Identification and evaluation of the main experimental issues related to the use of xanthan gum solutions. The characterized length scale was not analyzed
Abou Najm and Atallah (2016)	Development of an alternative porosimetry method based on the injection of non-Newtonian fluids without yield stress: the ANA method. The obtained solutions are not unique, and the injection of several fluids is required
Malvault et al. (2017)	The authors proved that the accuracy of the YSM results could be substantially improved by considering the axial variation in the cross section of the pores
Rodríguez de Castro et al. (2018)	Effects of polymer concentration on the accuracy of YSM tests and sensitivity of the method to errors in rheological characterization of the fluid
Rodríguez de Castro et al. (2019)	Experimental characterization of packs of spherical beads by using YSM. Comparison to MIP and to the pore network as extracted from a 3D image of the media
Atallah and Abou Najm (2019)	Experimental validation of the 'ANA' method. The uniqueness of solution is not guaranteed in all cases
Rodríguez de Castro et al. (2020a)	Application of YSM through direct numerical simulations allowing the computation of PSD from an image of the medium. Good agreement with MIP and pore network modelling
Rodríguez de Castro et al. (2020b)	Extension of YSM to rough-walled rock fractures. Modelling aspects, numerical experiments and experimental validation
Mackaya et al. (2021)	Improvement of the bundle-of-capillaries model used in YSM by including triangular and rectangular pores

consists of a yield stress τ_0 followed by a shear-rate dependent viscosity, and is expressed as:

$$\begin{cases} \tau = \tau_0 + k\dot{\gamma}^n & \text{for } \tau \geq \tau_0 \\ \dot{\gamma} = 0 & \text{for } \tau \leq \tau_0 \end{cases} \tag{1}$$

where τ is the shear stress and $\dot{\gamma}$ is the shear rate. The consistency and the flow index of the Herschel-Bulkley fluid are named k and n, respectively.

During a YSM test, a Herschel-Bulkley fluid is injected through the investigated porous medium at $N + 1$ different flow rates Q_j ($j = 1 \ldots N + 1$), and the steady-state pressure gradient

∇P_j corresponding to each value of Q_j is measured. Therefore, the input data for the PSD calculation algorithm are a set of $(Q_j, \nabla P_j)$ data, and the rheological parameters τ_0, k and n.

Assuming a bundle-of-capillaries model with horizontal cylindrical pores, the pore size class representing the radius of the newly incorporated pores contributing to the total flow rate Q_i under a given pressure gradient ∇P_i is defined as:

$$r_i = \alpha \frac{2\tau_0}{\nabla P_i} \ (i = 1...N) \tag{2}$$

It is essential to understand that the onset pressure gradient at which a yield stress fluid starts to flow through a pore of radius r is $\nabla P = \frac{2\tau_0}{r}$. Therefore, only the pores with $r > \frac{2\tau_0}{\nabla P_i}$ produce a significant contribution to the total flow rate Q_i under a pressure gradient ∇P_i. The value of α in Eq. (2) must be strictly greater than unity, because the contribution of the pores with $r = \frac{2\tau_0}{\nabla P_i} (\alpha = 1)$ is not noticeable at ∇P_i. Rodríguez de Castro et al. (2014) described the procedure used to determine the value of α, ensuring the unicity of the solution in terms of PSD.

In the YSM inversion method, the number of pores n_i belonging to each pore radius class r_i is calculated as being the maximum positive integer respecting all the following conditions:

$$Q_s \ge \sum_{g=1}^{i} n_g q(\nabla P_s, r_g) \quad \text{for} \quad s \ge i+1 \tag{3}$$

In the preceding equation, $q(\nabla P_s, r_g)$ is the volumetric flow rate of a Herschel-Bulkley fluid through a cylindrical capillary of radius r_g under a pressure gradient ∇P_s (expression given by Skelland 1967 and Chhabra and Richardson 2008). The determination of n_j starts from n_1 (the number of the biggest pores), and then continues with n_2, n_3, etc., until the number of the smallest pores n_N is calculated.

It should be noted that, according to Eq. (3), the number of pores n_i of a given pore class r_i is constrained by $(N + 1 - i)$ conditions. Therefore, the smallest pore classes associated to the highest pressure gradients are more sensitive to experimental uncertainties. In order to solve this issue, the four highest experimental ∇P_j data were fitted to a power-law of Q, expressed as $f(Q) = aQ^b$. Then, the relative deviation with respect to such a fit was calculated for all $(Q_j, \nabla P_j)$ data points as $e(j) = \left| \frac{[f(Q_j) - \nabla P_j]}{f(Q_j)} \right|$, and the number of pores n_j of the class r_j was neglected unless $e(j) > 0.05$. In other words, the frequency of the pores in which stagnation of the yield stress fluid did not result in a >5% increase of the pressure gradient was neglected. Next, the relative frequency of each pore class r_i, named $p(r_i)$, can be calculated as:

$$p(r_i) = \frac{n_i}{\sum_{s=1}^{N} n_s} \tag{4}$$

The standard version of YSM will be used in the present investigation, which assumes that all pores are cylindrical; however, a recent work has been presented in which the impact of considering triangular, square and circular cross-sections of the pores on the PSD provided by YSM has been assessed (Mackaya et al. 2021). As explained in this previous work, the distribution of shape factors in a porous sample is unknown unless some pore-network modeling is performed based on a digital image of the investigated material. However, this information is not readily available from YSM and requires either additional imaging tests such as 3D microcomputed tomography, or the use of literature results. In order to assess the performance of YSM independently, without any extra input from other methods, cylindrical pores are assumed in the present work.

Experimental procedures

Investigated porous media

Three different porous media were investigated in the current work: an artificial A10 sintered silicate, and two different natural sandstones, a Bentheimer sandstone and a Berea sandstone. A10 sintered silicate is a consolidated synthetic porous medium of high permeability and porosity produced by fusing graded silica powders. Its constituents are mainly silica (~90%) and alumina (~5%), with small quantities of other oxides. This material has been frequently used in previous research (e.g., Eilertsen et al. 1997; Pentland 2010; Fleury 2018), given that A10 cores exhibit ranges of pore-throat size distributions, porosities and permeabilities that are comparable to those of sand packs of uniform grain sizes, with the advantage of being consolidated and reproducible. The petrophysical characteristics of A10 silicates can be consulted in the work of Hamon and Vidal (1986).

Bentheimer sandstone was deliberately selected because of its suitable characteristics for laboratory experiments and the associated comparison with theoretical models, i.e., a constant mineralogy and a block-scale homogeneous nature in terms of grain size distribution, porosity and permeability. Also, the widespread use of this ideal sedimentary rock in a variety of reservoir topics ranging from transport in the groundwater zone and environmental remediation to geothermal energy production makes it an attractive candidate for comparative experimental works. Together with the composition of Bentheimer sandstones, Peksa et al. (2015) reviewed the transport properties of these rocks, reporting the ranges of porosity, permeability, grain size distribution, pores bodies and throat-size distributions obtained

by means of different techniques, including MIP, X-ray microtomography and statistical reconstruction of 2D thin section images.

Berea sandstone is also widely used as a model rock for studying fluid flow through porous media, due to the consistent petrophysical properties of the cores cut from the same batches of the quarried stone, and the different permeabilities obtained from cores cut from different zones of the quarry (Ma and Morrow 1994). This type of rock is made up of well-sorted and well-rounded predominately quartz grains, but it also contains minor amounts of feldspar, dolomite, and clays (Churcher et al. 1991; Ma and Morrow 1994). The petrophysical characteristics of different Berea sandstones were reported in previous research (Churcher et al. 1991; Øren and Bakke 2003; Ribeiro Cardoso and de Carvalho Balaban 2015; Kareem et al. 2017).

A set of cylindrical samples was used to perform the YSM flow experiments presented in the following subsection. The length (L) taken for the measurement of the pressure drop ΔP_j (with $\nabla P_j = \frac{\Delta P_j}{L}$) over each investigated sample, as well as the diameter D, the absolute permeability K and the porosity ε of each core are listed in Table 2. It can be observed that the permeability values extended over more than two decades. The polymer concentration C_p of the injected xanthan gum solution and the number of experimental measurements $N + 1$ is also provided.

YSM laboratory tests

Two aqueous xanthan gum solutions with polymer concentrations C_p of 9,000 and 10,000 ppm were prepared to be used as injected yield stress fluids. Once prepared, the fluids were degassed using a vacuum pump. The bulk rheological parameters of these fluids were empirically determined from stress vs. shear rate measurements performed with a cone-and-plate rheometer. These measurements are represented in Fig. 1.

The values of τ_0, k and n obtained by fitting the experimental data to Eq. (1) were $\tau_0 = 13.74$ Pa; $k = 0.206$ Pa s^n and $n = 0.66$ for the 9,000-ppm solution and $\tau_0 = 14.18$ Pa; $k = 0.443$ Pa s^n and $n = 0.56$ for the 10,000-ppm solution. As expected, higher values of C_p led to higher values of τ_0 and k and more marked shear-thinning effect (lower values of n). The uncertainty in the experimentally measured values of τ_0,

k and n was determined through evaluation of the goodness of fit of the measured rheogram to the reconstructed one (Hershel-Bulkley model with the obtained parameters). For the investigated fluids, the relative standard deviations were close to ±2% for τ_0, ±11% for k and ± 2% for n.

A simple experimental setup was used to conduct the yield stress fluids injection tests, in which the cylindrical cores, introduced in subsection 'Investigated porous media', were coated with a nonwetting epoxy resin and then wrapped with epoxy-coated fiberglass to insure liquid imperviousness and mechanical strength. Aluminium injector plates were installed at the inlet and the outlet of the cores. The inner surface of these injector plates, which are in contact with the cores, were coated with Teflon in order to prevent any ion exchange between the metal and the core. A syringe pump was used to inject the Herschel-Bulkley fluid at a controlled flow rate, and the pressure drop measurements were performed by means of a differential pressure sensor over the lengths (L) listed in Table 2. The injection circuit was open, and the effluent was collected using a vessel.

During each experiment, a set of different flow rates Q_j ($j = 1…N + 1$) were imposed to the injected yield stress fluid, in accordance with the following sequence:

$$Q_j = Q_{min} \left(\frac{Q_{max}}{Q_{min}} \right)^{\left(\frac{N+1-i}{N} \right)} \tag{5}$$

with $Q_{min} = 0.01$ ml/h, $Q_{max} = 1,000$ ml/h and $N + 1$ being the number of experimental measurements. In each step, the fluid was injected at the predefined flow rate Q_j and the steady-state pressure drop ΔP_j was measured. Then, the flow rate was steeply decreased to Q_i and the same procedure was repeated until the whole (Q, ΔP) dataset was obtained. The relative standard deviation of the pressure drop measurements was 8% for $Q < 1$ ml/h, 1% for 1 ml/h $< Q <$ 150 ml/h and 0.5% for $Q > 150$ ml/h. The room temperature was kept constant at 20 °C ± 0.1 °C during all the experiments. The number of experimental data as well as the C_p of the injected solution for each core are given in Table 2.

From the obtained (Q_j, ΔP_j) raw experimental data, the YSM inversion algorithm described in section 'YSM porosimetry method: PSD calculation algorithm' was applied, allowing for the determination of the PSD of each porous

Table 2 Length L taken for the measurement of the pressure drop, diameter D, absolute permeability K and porosity ε of each porous sample used in the flow experiments

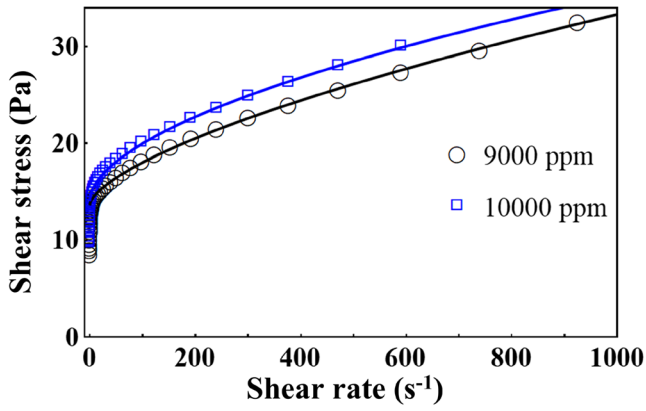| Sample	L [cm]	D [cm]	K [m^2]	ε [−]	C_p [ppm]	$N+1$ [−]
A10 sintered silicate	6.3	4.7	8.22×10^{-12}	0.51	10,000	50
Bentheimer sandstone	4.7	4.7	2.87×10^{-12}	0.23	9,000	50
Berea sandstone	5.0	3.8	3.75×10^{-14}	0.22	7,000	34

Fig. 1 Rheograms of the xanthan gum solutions for the two different values of polymer concentration. Symbols represent experimental data, while solid lines correspond to Herschel-Bulkley fits (Eq. 1)

medium. It must be highlighted that the experimental data corresponding to the Berea sandstone sample were taken from the literature (Rodríguez de Castro et al. 2016). The Herschel-Bulkley parameters of the 7,000 ppm xanthan gum solutions used in that case were $\tau_0 = 9.61$ Pa, $k = 0.430$ Pa s^n and $n = 0.55$.
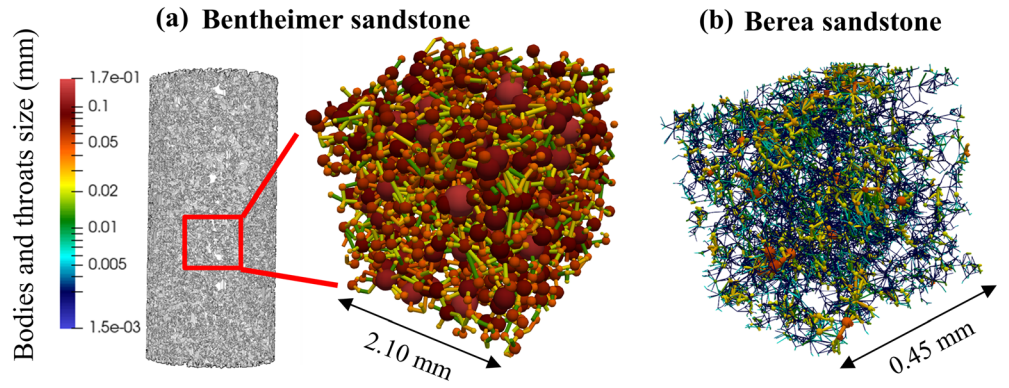
Pore network extraction

Pore networks consisting of a set of spherical pores bodies interconnected by cylindrical pore throats were generated for each investigated porous medium, as a simplified representation of the actual geometry of the pore space. In the procedure used to extract the pore network from digital images of the three investigated porous media, the subnetwork of the oversegmented watershed (SNOW) algorithm (Gostick 2017) was used. In SNOW, the distance map of the void spaces is first extracted and is subsequently filtered by eliminating the peaks on saddles and plateaus. The neighbour peaks are then merged and void voxels are assigned to pore bodies. This algorithm is included in the open-source toolkit for quantitative analysis of porous media images, PoreSpy (Gostick et al. 2019).

The freely available 3D microcomputed tomography image of a dry Bentheimer sandstone core provided by Ramstad (2018), which was imaged with 6.67-μm resolution, was used to extract the pore network model of this type of rock. A 2.10 × 2.10 × 2.10-mm³ cubic volume was used for the generation of the pore network, as shown in Fig. 2a. The experimentally measured values of absolute permeability and porosity of the imaged Bentheimer sample were close to 2,900 mD and 23%, respectively (Ramstad et al. 2012). Furthermore, a 1.38-mm diameter cylindrical sample of Berea sandstone, analogous to the one used in the experiments presented in the preceding subsection (coming from the same batch of cores and from the same provider), was imaged in the present work by means of a micro computed tomography device, providing a 3D

image of the sample microstructure. The voxel size of the obtained digital image was 1.50 μm, and the scanned volume had 1.38 × 1.38 × 1.38-mm³ dimensions. The dimensions of the cubic volume used for the generation of the pore network were of 450 × 450 × 450 μm³ in this case, as shown in Fig. 2b. Other researchers used volumes of similar size when extracting the pore network models of Berea sandstones, (e.g., Sharqawy 2016 used 500 × 500 × 500 μm³ and Thomson et al. 2018 used 370 × 370 × 370 μm³). Moreover, based on the results of synchrotron datasets obtained at a spatial resolution of 0.74 μm, Chauhan et al. (2020) recommended a representative elementary volume of at least 355 × 355 × 355 μm³ for Berea sandstone. Regarding the A10 sintered silicate, a thin sample (8 mm diameter) of this material (also coming from the same batch of cores and from the same provider) was imaged in the work of Rodríguez de Castro (2014) using microcomputed tomography. The scanned volume had 3 × 3 × 6-mm³ dimensions, and the voxel size was 3.29 μm. However, only a 2D image was published in the previous work, so a slice of 2.04 × 2.04 mm² dimensions was taken in the present work to generate the pore network, as shown in Fig. 3.

Previous efforts were devoted to study the effect of resolution on the extracted pore and throat size distributions for consolidated porous media. In the work of Peng et al. (2012), two different resolutions of 12.7 and 0.35 μm were used for the acquisition of X-ray computed microtomography images of a Berea sandstone, and the results were compared with those of an MIP test. By doing so, the authors assessed the impact of resolution on several pore structure parameters, including porosity, PSD, and pore connectivity. Their results showed that the selection of a proper resolution should be based on the PSD of the sample. They proposed a resolution of 1.85 μm for their Berea sandstone, which had a volume-averaged pore size of 20 μm as measured by MIP. Leu et al. (2014) used a 2.99-μm resolution for the analysis of a Berea sandstone sample and recommended basing the validation of image processing workflows on permeability values. In their work, microtomography measurements were conducted both on the dry rock, and during drainage and imbibition cycles of two-phase fluids. Their results proved that microporous regions below imaging resolution did not contribute significantly to the flow behavior. Moreover, Alyafei et al. (2015) performed microtomography experiments on two sandstones and two limestones. For the Berea sandstone, they tested different resolutions ranging from 2.77 to 22.16 μm, and calculated porosity and permeability on these images by using direct simulation and by extracting geometrical equivalent networks. The authors showed that the predicted porosity in sandstones is roughly insensitive to resolution within the selected range, and that comparable permeability values are obtained independently of the voxel size. Also, with the aim to check the appropriateness of the used resolution, they proposed

Fig. 2 Illustration of the pore network models extracted from the two porous media investigated in the present work: **a** Bentheimer sandstone and **b** Berea sandstone

comparing the average throat size of the extracted pore network to the one obtained by MIP, or alternatively compare the measured and imaged porosity and ensure that the segmented image captures more than 90% of the porosity. For all the porous media investigated in the present study, it was checked that both the porosity and the permeability values of the imaged cores were very close to the experimentally measured values of the cores used in the flow experiments (listed in Table 2). The limitations in terms of resolution are expected to be more restrictive in the case of the Berea sandstone sample, as it presents the smallest pore sizes among the three analyzed porous media. On this subject, it can be remarked that the resolution used when imaging the current Berea sandstone sample (voxel size of 1.50 μm) was close to the values recommended in the previously mentioned works. A great number of previous works exist dealing with the application of X-ray to characterize the microstructure of porous media, and the details on the advantages and limitations of this technique can be consulted in the literature (Lindquist and Venkatarangan 2000; Burlion et al. 2006; Prodanovic et al. 2006; Karpyn et al. 2007; Wildenschild and Sheppard 2012; Bultreys et al. 2016; Li et al. 2017; Houston et al. 2017; Tembely et al. 2019).
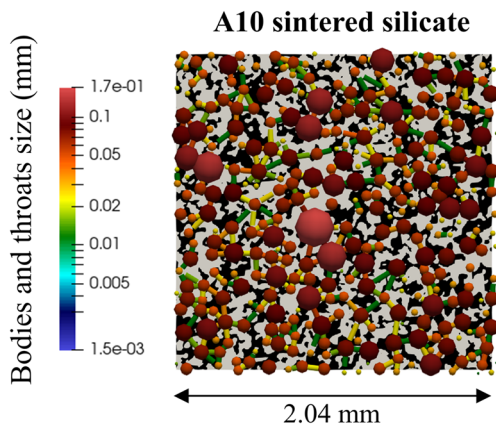

Fig. 3 Illustration of the pore network model extracted from the 2D image of the A10 silicate. Black colour represents solid and light grey colour represent pores

MIP laboratory tests

As reported by Peksa et al. (2015), the mercury intrusion technique and its interpretation underestimate the large pores and overestimate the small pores. As the large pore bodies can be surrounded by pore throats and smaller pore bodies, the PSD provided by MIP defines the volume fraction of pores that are accessible through pore openings of a given size (Cieszko et al. 2019). Rouquerol et al. (2012) reviewed the limitations and operating conditions of some porosimetry methods used to characterize porous materials having pore widths in the macropore range of 50–500 μm, including MIP and X-ray microtomography. Moreover, Jiao et al. (2020) recently reviewed the latest applications and improvement of MIP, discussing the limitations and future directions for this technique. In particular, the maximum mercury intrusion capillary pressure applied during an MIP experiment is of approximately 276 MPa, which means that mercury theoretically enters a minimum pore opening radius as small as 2.7 nm (Jiao et al. 2020; Wang et al. 2018).

An automated mercury porosimeter was used to conduct MIP tests on a sample of each porous medium investigated in the present work. The raw results of the mercury intrusion tests provided, for each porous sample, the increase in invading phase (mercury) saturation when the applied pressure P_c is increased. The applied P_c ranged from 3.6×10^{-2} to 4.1×10^3 bar for the Bentheimer and the Berea sandstone samples, and from 3.6×10^{-2} to 4.1×10^3 for the A10 silicate sample.

The radius r_i of the pore openings that are invaded at a given pressure P_c is given by (Washburn 1921):

$$r_i = -\frac{2\sigma \cos\theta}{P_{ci}} \tag{6}$$

In Eq. (6), the contact angle θ was assumed to be 140°, and the value $\sigma = 0.48$ Nm^{-1} was used for the surface tension of the mercury-air pair. These are routinely used values and are commonly accepted by most researchers (Giesche 2006). The mercury phase saturation under a pressure P_{ci} was named S_i,

and the volume-weighted frequency associated to the pore radius class r_i was calculated as:

$$p(r_i) = \frac{S_i - S_{i-1}}{S_Z} \tag{7}$$

with $i = 1 \ldots Z$ and $S_0 = 0$. It should be noted that the mercury intrusion stage can be expanded by an extrusion process (in which the extruded mercury volume is measured while the pressure is progressively decreased). However, the information determined by the extrusion step is not widely used due to numerous open questions involved (Voigt et al. 2020).

Results

Raw experimental measurements

Figure 4 displays the raw $(Q_i, \nabla P_i)$ experimental data obtained during the YSM tests conducted in the present investigation. The relative standard deviation of the pressure drop measurements was 8% for $Q < 1$ mL/h, 1% for 1 mL/h $< Q <$ 150 mL/h and 0.5% for $Q > 150$ mL/h. It can be observed that the relationship between Q and ∇P is clearly non-linear as a result of both the shear-thinning behaviour of the injected solutions and the increasing number of pore classes contributing to fluid flow as ∇P increases. Moreover, the range of pore radius classes explored in each test was also calculated through Eq. (2), obtaining 9.32 to 49.58 μm for the A10 sintered silicate and 7.79–44.62 μm for the Bentheimer sandstone. Smaller pore radii can be explored by increasing the injection flow rate, within the limits of negligible polymer retention. It is reminded that the experimental data corresponding to the Berea sandstone sample displayed in Fig. 4c were taken from the literature (Rodríguez de Castro et al. 2016). The explored pore radius range was from 0.48 to 9.92 μm in the case of the Berea sandstone experiment.

PSDs provided by YSM and MIP

The inversion algorithm described in section 'YSM porosimetry method: PSD calculation algorithm' was used to extract the PSDs of the three investigated porous media from the raw $(Q_i, \nabla P_i)$ experimental data displayed in Fig. 4. The results are shown in Fig. 5 and are also compared to the results provided by MIP. Furthermore, the differences in terms of the average pore radius size are listed in Table 3. It is first noted that broad agreement was found between the results provided by MIP and YSM, both in terms of pore radii ranges and average pore radius classes. A conspicuous feature of this comparison is that, while YSM provides slightly greater pore sizes than MIP for the A10 silicate and

the Bentheimer sandstone, the PSDs are shifted towards small pores in the case Berea sandstone. This is consistent with the results of the numerical experiments performed by Rodríguez de Castro et al. (2020a) on unconsolidated porous media. In the previous work, it was observed that YSM yielded slightly larger pore sizes than MIP for porous media displaying wide PSDs due to the existence of preferential flow paths for the yield stress fluid avoiding the smallest constrictions. These numerical results were confirmed by the experimental observations provided by the YSM tests performed on packs of spherical beads (Rodríguez de Castro et al. 2019), for which slightly larger pore sizes were also obtained by YSM as compared to MIP. This is also expected to be the case of the A10 sintered silicate and the Bentheimer sandstone analyzed in the present work, which present a larger statistical dispersion of their PSDs than Berea sandstone, as will be shown in the following subsection.

Analysis of the obtained pore-size distributions through comparison with pore network modeling

The pore-body size distributions (BSDs) and pore-throat size distributions (TSDs) extracted from the digital images of the three investigated media following the procedure described in subsection 'Pore network extraction' are presented in Fig. 6 and are compared with the results obtained from the YSM tests. It is clear from these results that the TSD and BSD of Berea sandstone are very similar and almost overlap (in good agreement with the results of Peksa et al. 2015). The difference between TSD and BSD is more marked in the case of the A10 silicate and the Bentheimer sandstone, which can result in the generation of preferential fluid paths. The same figure shows that the YSM results fall within the range in which the TSD and the BSD overlap for the A10 silicate and the Bentheimer sandstone. In the case of the Berea sandstone, the YSM yields PSDs that are within the range of TSD and BSD. In all cases, the PSDs obtained by YSM is closer to the size of the pore throats than to the size of the pore bodies, due to the strong influence of the constrictions on the generation of pressure losses throughout the media. In this respect, it is underscored that pressure loss is the measured quantity in YSM tests. The differences between the TSD obtained from pore network modeling and the PSD provided by YSM and MIP are listed in Table 3. From this table, it may be concluded that YSM approximates reasonably well the TSD for these porous media, and particularly good agreement is obtained for the Berea sandstone in terms of the average pore size. Moreover, the PSD provided by the three porosimetry methods are compared in Fig. 7, showing that the range of pore sizes provided by both MIP and YSM fall within the range of the TSD. The differences between the average pore sizes provided by the three investigated methods are lower than 28% for the A10 silicate and the Bentheimer sandstone
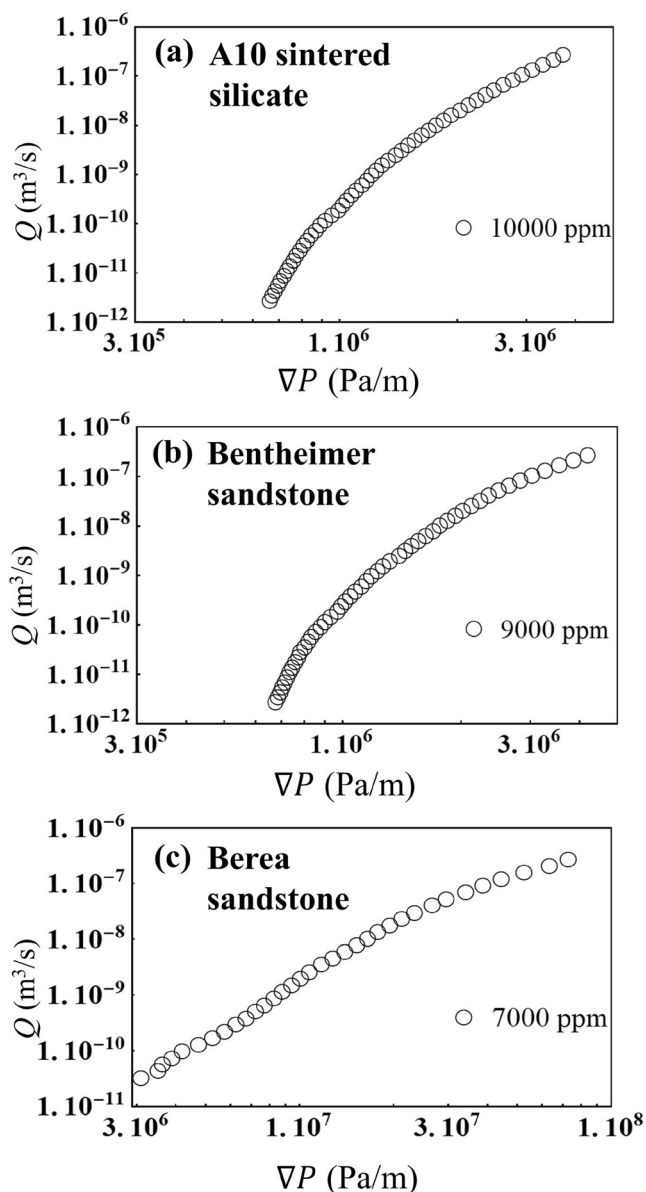
Fig. 4 Flow rate vs. pressure gradient experimental measurements obtained during the YSM laboratory tests: **a** A10 sintered silicate, **b** Bentheimer sandstone and **c** Berea sandstone

pore size distribution, in which only a single characteristic length is used to describe the dimensions of the pores. Moreover, the use of a single length is only possible through the decomposition of the complex microscopic geometries into a set of elements with regular shape, which is no more than a useful idealization—for example, MIP assumes a bundle-of-capillaries model in which the actual sizes of the pores are assimilated to the size of the pore openings (pore throats providing access to a portion of the pore volume). When the injection pressure is higher than the capillary threshold pressure corresponding to the pore opening, the pores are invaded by mercury; therefore, the injection pressure in MIP is equivalent to the capillary pressure, and the capillary radius is considered to be the pore radius (Giesche 2006; Jiao et al. 2020). As explained in section 'YSM porosimetry method: PSD calculation algorithm', a bundle-of-capillaries model is also assumed in YSM. The radii of the pores provided by YSM are closely related to the size of the pore constrictions, as shown by the numerical results of Rodríguez de Castro et al. (2020a) and the experimental results of the present study. In the case of microtomography, pore networks consisting of a set of spherical pores bodies interconnected by cylindrical pore throats are extracted from digital images, as presented in section 'YSM laboratory tests'. In the current work, the TSDs and BSDs provided by pore network modeling correspond to the distributions of the inscribed diameters of the pore bodies and the pore throats, respectively. It must be highlighted that, while both the YSM and MIP are assuming the pore space is a bundle of capillary tubes, the pore network extraction from digital rock images does not share the same assumption; therefore, a direct comparison is not straightforward. In this sense, a recent numerical work used pore network modeling to simulate the flow of shear-thinning fluids in model porous media (Rodríguez de Castro and Goyeau 2021). The results of these works showed that pressure drop at the Darcy scale, which is the measured quantity in YSM, is mainly sensitive to the viscosity exhibited by the fluid in the active flow channels, i.e., the flow channels in which the flow rate is not negligible. When injecting a yield stress fluid, as in YSM tests, a channel is active or not under a given pressure gradient depending on the size of the pore throats.

Readers are reminded that the result of MIP represents the volume fraction of pores that are accessible through pore openings of a given size (Giesche 2006; Jiao et al. 2020). MIP is therefore sensitive to the largest openings to pore bodies. The sizes of the largest pore openings are not exactly identical to the size of the pore throats. On the other hand, YSM provides the radii of the cylindrical capillaries in a bundle of capillaries having the same length and giving the same pressure drop as the actual porous medium under any flow rate; therefore, the dimension provided by YSM is more closely related to the hydrodynamic radius than the throat radius.
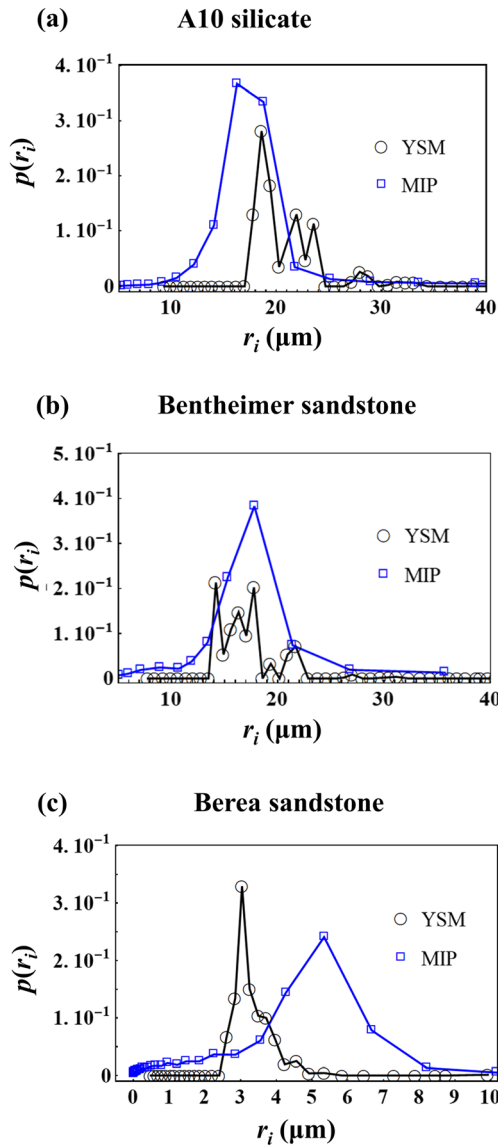
samples. As listed in Table 3, the most important difference in relative terms is observed between the average pore size obtained with MIP for the Berea sandstone and the ones obtained with the other two methods. The fact that smaller pore sizes are obtained with YSM as compared to MIP for Berea sandstone may stem from the reasons discussed in subsection 'PSDs provided by YSM and MIP' (narrower PSD as compared to A10 and Bentheimer).

It must be borne in mind that the three porosimetry methods used in the current work assume simplified geometries of the pores, which is understandable given the continuous and irregular nature of the connected pore space. Such a continuous pore space needs to be discretized when defining a

Fig. 5 PSDs provided by YSM and MIP. **a** A10 sintered silicate, **b** Bentheimer sandstone and **c** Berea sandstone
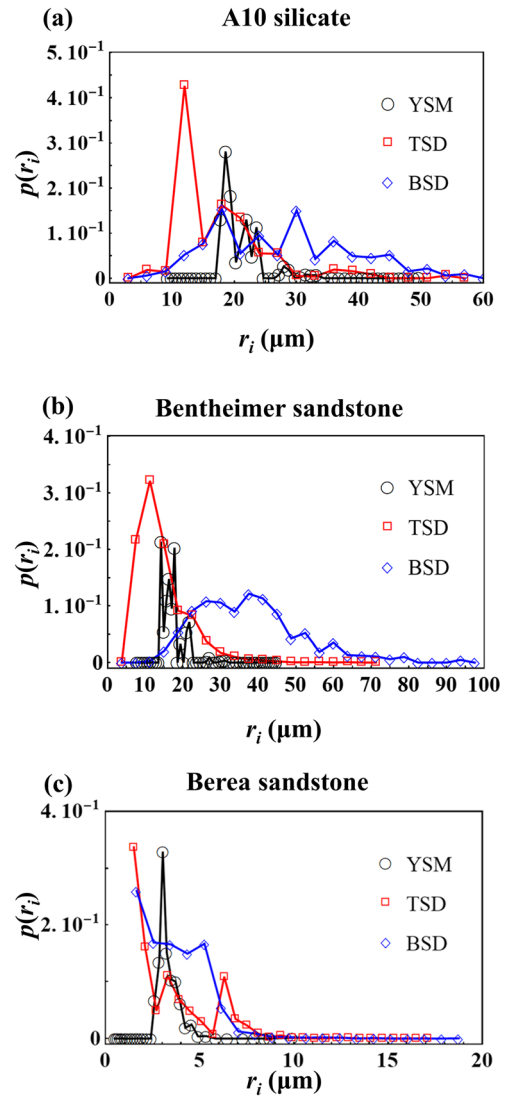

Fig. 6 Comparison between the PSDs provided by YSM and the TSDs and BSDs obtained by using the pore network modelling approach, for all the injected yield stress fluids: **a** A10 sintered silicate, **b** Bentheimer sandstone and **c** Berea sandstone

The differences between pore throat radius, hydrodynamic radius, and pore opening radius were discussed in the past, for example in the work of Chauveteau et al. (1996). Chauveteau et al. (1996) studied the relationship between the equivalent hydrodynamic diameter of a pore d_h and the

pore opening diameters derived from MIP tests d_{Hg} in sandstones. d_h is the diameter of a cylindrical capillary having the same pore length and giving the same pressure drop as the actual pore for a considered flow rate. As stated by Chauveteau et al. (1996), independently of the refinement of

Table 3 Average pore sizes provided by the different porosimetry methods: YSM, MIP and throat-size distribution (TSD) obtained with pore network modelling. The differences between YSM and MIP (Diff YSM-MIP), between YSM and TSD (Diff YSM-TSD) and between MIP and TSD (Diff MIP-TSD) are also listed

Sample	Average (MIP)	Average (TSD)	Average (YSM)	Diff YSM-MIP (%)	Diff YSM-TSD (%)	Diff MIP-TSD (%)
A10	16.28	17.29	20.78	27.64	20.18	−5.84
Bentheimer	15.14	14.44	17.05	12.62	18.07	4.85
Berea	5.17	3.33	3.27	−36.75	−1.80	55.26

(a) A10 silicate
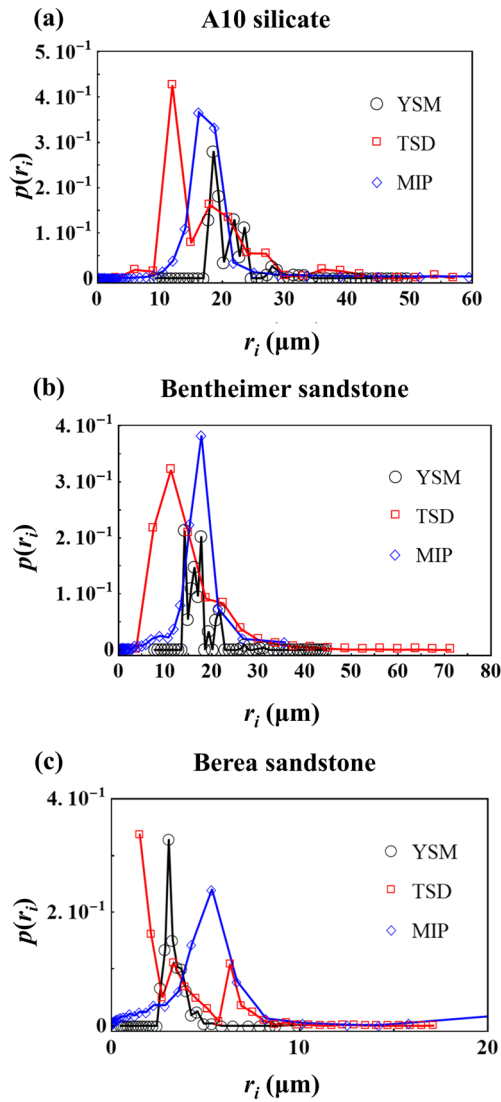
(b) Bentheimer sandstone

(c) Berea sandstone

Fig. 7 Comparison of the PSD provided by YSM (black circles), the PSD obtained with MIP (blue diamonds) and the TSD of the extracted pore network model (red squares) for the three porous media: **a** A10 sintered silicate as obtained with C_p = 10,000 ppm and **b** Bentheimer sandstone as obtained with C_p = 9,000 ppm and **c** Berea sandstone as obtained with C_p = 7,000 ppm

the analysis process, mercury intrusion remains a static non-directional process. Mercury invades pore bodies by the largest pore throats while the directional character of fluid flow implies the preferential use of pore throats located upstream and downstream. Thus, the equality between pore dimensions determined by mercury injection and flow experiments would be obtained only for unrealistic porous media where all pore throats would have the same size.

Conclusion

The PSDs provided by YSM and MIP have been compared, for the first time, with those obtained from pore network

modelling for three consolidated porous media, finding, in general, a good agreement between the three methods. The current results elucidate the physical meaning of the characterized pore dimension with YSM, showing that the PSDs obtained by YSM are closer to the pore throat than to the pore body radii. It has been shown that the length scale provided by YSM is relevant to the prediction of contaminant transport in porous media, as TSD is closely related to particle straining and contaminant phase displacement. In this sense, the results of YSM can be useful to estimate the maximum elongation rates over a flow path, which are associated to mechanical degradation of polymer solutions and other complex fluids used in soil remediation applications. Knowledge of TSD is also important in the applications in which underground storage of liquids and gases are involved.

Furthermore, YSM was able to scan pore sizes ranging from 0.48 to 49.58 μm in the present experiments, being able to analyse samples with permeability values extending over more than two decades. General agreement was found between the results provided by MIP and YSM in the investigated consolidated porous media, both in terms of pore radii ranges and average pore radius classes. It should be noted that the occurrence of preferential flow paths consisting of connected networks of high conductance pores is uncommon in the case of naturally consolidated porous materials of moderate permeability for which the BSD and TSD overlap, such as the analyzed Berea sandstone. This contrasts with the case of the A10 silicate, which is an extremely porous artificially sintered medium, and to some extent with the case of the highly permeable Bentheimer sandstone. In this regard, the results of previous numerical works were experimentally validated, showing that YSM yields slightly larger pore sizes than MIP in the presence of preferential flow paths, while smaller pore sizes are obtained in the case of sandstones with more complex pore geometries, as a consequence of the tortuous flow paths which go through the smallest pore throats. Indeed, the PSDs provided by YSM for the investigated porous media fell within the region in which BSD and TSD overlap.

The efficiency of YSM when applied to low-permeability consolidated media is an issue for further consideration. Further research should focus on the formulation of yield stress fluids by using only nanometric constituent particles, which would open the way for replacement of MIP. Moreover, prospective works should also be undertaken to assess the accuracy of YSM when characterizing porous media with dual permeability. In this sense, a suitable injection fluid must be identified allowing for the experimental characterization porous media with smaller pore sizes. This fluid must not modify the internal geometry and morphology of the pores, e.g., through polymer adsorption or retention. Furthermore, previous works showed that different porosimetry methods should be combined to characterize the

PSDs of porous media having a wide range of pore sizes (Bultreys et al. 2016; Jiao et al. 2020), such as tight reservoir rocks (Wang et al. 2018), some types of sandstones (Tsakiroglou and Payatakes 2000) and shales (Chen et al. 2018; Alfi et al. 2019). For example, MIP data sets, scanning electron microscopy images, percolation-type approaches and inverse modeling algorithms were combined in the past to characterize the microstructure of heterogeneous mineral soils and reservoir rocks (Tsakiroglou and Ioannidis 2008; Tsakiroglou et al. 2009; Amirtharaj et al. 2011). Additionally, the N_2 adsorption porosimetry method was combined with MIP in a recent work to characterize the PSDs of several shale samples (Liu and Ostadhassan 2019).

Declarations

References

Abou Najm MR, Atallah NM (2016) Non-Newtonian fluids in action: revisiting hydraulic conductivity and pore size distribution of porous media. Vadose Zone J 15(9):1539–1663

Aizebeokhai AP, Oyeyemi KD (2018) Geoelectrical characterisation of basement aquifers: the case of Iberekodo, southwestern Nigeria. Hydrogeol J 26:651–664

Alyafei N, Qaseminejad Raeini A, Paluszny A, Blunt MJ (2015) A sensitivity study of the effect of image resolution on predicted Petrophysical properties. Transp Porous Media 110:157–169

Alfi M, Barrufet M, Killough J (2019) Effect of pore sizes on composition distribution and enhance recovery from liquid shale: molecular sieving in low permeability reservoirs. Fuel 235:1555–1564

Ambari A, Benhamou M, Roux S, Guyon E (1990) Distribution des tailles des pores d'un milieu poreux déterminée par l'écoulement d'un fluide à seuil [Distribution of the pore sizes of a porous medium determined by the flow of a threshold fluid]. C R Acad Sci Paris 311 (II): 1291–1295

Amirtharaj ES, Ioannidis MA, Parker B, Tsakiroglou CD (2011) Statistical synthesis of imaging and porosimetry data for the characterization of microstructure. Transp Porous Media 86(1):135–154

Atallah NM, Abou Najm MR (2019) Characterization of synthetic porous media using non-Newtonian fluids: experimental device. Eur J Soil Sci 70:257–267

Ball WP, Buehler C, Harmon TC, Mackay DM, Roberts PV (1990) Characterization of a sandy aquifer material at the grain scale. J Contam Hydrol 5:253–295

Bloomfiel JP, GooddyD C, Bright MI, Williams PJ (2001) Pore-throat size distributions in Permo-Triassic sandstones from the United Kingdom and some implications for contaminant hydrogeology. Hydrogeol J 9:219–230

Blunt MJ, Bijeljic B, Dong H, Gharbi O, Iglauer S, Mostaghimi P, Pentland C (2003) Pore-scale imaging and modelling. Adv Water Resour 51:197–216

Bradford SA, Kim HN, Haznedaroglu BZ, Torkzaban S, Walker SL (2009) Coupled factors influencing concentration-dependent colloid transport and retention in saturated porous media. Environ Sci Technol 43:6996–7002

Bultreys T, De Boever W, Cnudde V (2016) Imaging and image-based fluid trans- port modeling at the pore scale in geological materials: a practical introduction to the current state-of-the-art. Earth Sci Rev 155:93–128

Burlion N, Bernard D, Chen D (2006) X-ray microtomography, application to microstructure analysis of a cementitious material during leaching process. Cem Concr Res 36:346–357

Chhabra RP, Richardson JF (2008) Non-Newtonian flow and applied rheology: engineering applications. Butterworth-Heinemann, Boston; Elsevier, Amsterdam

Chaplain V, Mills P, Guiffant G, Cerasi P (1992) Model for the flow of a yield fluid through a porous medium. J Phys II France 2:2145–2158

Chauhan S, Sell K, Rühaak W, Wille T, Sass I (2020) CobWeb 1.0: machine learning toolbox for tomographic imaging. Geosci Model Dev 13:315–334

Chauveteau G, Nabzar L, El Attar L, Jacquin C (1996) Pore structure and hydrodynamics in sandstones. SCA conference paper number 9607, Society of Core Analysts, Los Angeles, CA, 1996

Chen G, Lu S, Zhang J, Pervukhina M, Liu K, Wang M, Han T, Tian S, Li J, Zhang Y, Ch X (2018) A method for determining oil-bearing pore size distribution in shales: a case study from the Damintun Sag, China. J Petrol Sci Eng 166:673–678

Churcher PL, French PR, Shaw JC, Schramm LL (1991) Rock properties of Berea sandstone, baker dolomite, and Indiana limestone. Proceedings of SPE International Symposium on Oilfield Chemistry, Anaheim, CA, February 1991

Cieszko M, Kempinski M, Czerwinski T (2019) Limit models of pore space structure of porous materials for determination of limit pore size distributions based on mercury intrusion data. Transp Porous Media 127:433–458

Diamond S (2000) Mercury porosimetry: an inappropriate method for the measurement of pore size distributions in cement-based materials. Cem Concr Res 30:1517–1525

Eilertsen T, Børresen KA, Bertin H, Graue A (1997) Experiments and numerical simulations of fluid flow in a cross layered reservoir model. J Pet Sci Eng 18:49–60

Feng X, Zeng J, Zhan H, Hu Q, Ma Z, Feng S (2020) Resolution effect on image-based conventional and tight sandstone pore space reconstructions: origins and strategies. J Hydrol 586:124856

Fleury M (2018) Measurement of interfacial area from NMR time dependent diffusion and relaxation measurements. J Colloid Interface Sci 509:495–501

Giesche H (2006) Mercury porosimetry: a general (practical) overview. Part Part Syst Charact 23:1–11

Gostick JT (2017) Versatile and efficient pore network extraction method using marker-based watershed segmentation. Phys Rev E 96: 023307

Gostick JT, Khan ZA, Tranter TG, Kok MD, Agnaou M, Sadeghi M, Jervis R (2019) PoreSpy: a Python toolkit for quantitative analysis of porous media images. J Open Source Software 4:1296

Hamon G, Vidal J (1986) Scaling-up the capillary imbibition process from laboratory experiments on homogeneous and heterogeneous samples. SPE 15852, Proc SPE European Pet Conf, London, 20–22 October 1986

Hancock PJ, Boulton AJ, Humphreys WF (2005) Aquifers and hyporheic zones: towards an ecological understanding of groundwater. Hydrogeol J 13(1):98–111

Harvey RW, Garabedian SP (1991) Use of colloid filtration modeling movement of bacteria through a contaminated sandy aquifer. Environ Sci Technol 25:178–185

Houston AN, Otten W, Falconer R, Monga O, Baveye PC, Hapca SM (2017) Quantification of the pore size distribution of soils:

assessment of existing software using tomographic and synthetic 3D images. Geoderma 299:73–82

Jiao L, Andersen PØ, Zhou J, Cai J (2020) Applications of mercury intrusion capillary pressure for pore structures: a review. Capillarity 3:62–74

Kareem R, Cubillas P, Gluyas J, Bowen L, Hillier S, Christopher GH (2017) Multi-technique approach to the Petrophysical characterization of Berea sandstone core plugs (Cleveland quarries, USA). J Pet Sci Eng 149:436–455

Karpyn ZT, Grader AS, Halleck PM (2007) Visualization of fluid occupancy in a rough fracture using micro-tomography. J Colloid Interface Sci 307:181–187

Kueper BH, Abbott W, Farquhar G (1989) Experimental observations of multiphase flow in heterogeneous porous media. J Contam Hydrol 5:83–95

Leu L, Berg S, Enzmann F, Armstrong RT, Kersten M (2014) Fast X-ray Micro-tomography of multiphase flow in Berea sandstone: a sensitivity study on image processing. Transp Porous Media 105:451–469

Li X, Kang Y, Haghighi M (2018b) Investigation of pore size distributions of coals with different structures by nuclear magnetic resonance (NMR) and mercury intrusion porosimetry (MIP). Measurements 116:122–128

Li H, Li H, Wang K, Liu C (2018a) Effect of rock composition microstructure and pore characteristics on its rock mechanics properties. Int J Min Sci Technol 28(2):303–308

Li Z, Liu D, Cai Y, Ranjith PG, Yao Y (2017) Multi-scale quantitative characterization of 3-D pore-fracture networks in bituminous and anthracite coals using FIB-SEM tomography and X-ray μ-CT. Fuel 209:43–53

Lindquist WB, Venkatarangan A (2000) Pore and throat size distributions measured from synchrotron X-ray tomographic images of Fontainebleau sandstones. J Geophys Res Solid Earth 105(B9): 21509–21527

Liu K, Ostadhassan M (2019) The impact of pore size distribution data presentation format on pore structure interpretation of shales. Adv Geo-Energy Res 3:187–197

Ma S, Morrow NR (1994) Effect of firing on petrophysical properties of Berea sandstone. SPE-21045-PA, Society of Petroleum Engineers, Richardson, TX

Mackaya TE, Ahmadi A, Omari A, Rodríguez de Castro A (2021) Empirical flow rate/pressure drop relationships for non-circular capillaries used in yield stress fluid porosimetry. Transp Porous Media 136:587–605

Malvault G (2013) Détermination expérimentale de la distribution de taille de pores d'un milieu poreux par l'injection d'un fluide à seuil ou par analyse fréquentielle [Experimental determination of the pore size distribution of a porous medium by the injection of a threshold fluid or by frequency analysis]. PhD Thesis, Arts et Métiers ParisTech, Paris

Malvault G, Ahmadi A, Omari A (2017) Numerical simulation of yield stress fluid flow in capillary bundles: influence of the form and the axial variation in the cross section. Transp Porous Media 120:255–270

Miller JA (1999) Ground water atlas of the United States: introduction and national summary. US Geol Surv Hydrol Atlas 730-A

Mirabolghasemi M, Prodanović M, DiCarlo D, Ji H (2015) Prediction of empirical properties using direct pore-scale simulation of straining through 3D microtomography images of porous media. J Hydrol 529:768–778

Morris BL, Lawrence ARL, Chilton PJC, Adams B, Calow RC, Klinck BA (2003) Groundwater and its susceptibility to degradation: a global assessment of the problem and options for management. United Nations Environment Programme, New York

Nabawy BS, Géraud Y, Rochette P, Bur N (2009) Pore-throat characterization in highly porous and permeable sandstones. AAPG Bull 93(6):719–739

Oukhlef A (2011) Détermination de la distribution de tailles de pores d'un milieu poreux [Determination of the pore size distribution of a porous medium]. PhD Thesis, Arts et Métiers ParisTech, Paris

Oukhlef A, Champmartin S, Ambari A (2014) Yield stress fluids method to determine the pore size distribution of a porous medium. J Non-Newtonian Fluid Mech 204:87–93

Øren P-E, Bakke S (2003) Reconstruction of Berea sandstone and pore-scale modelling of wettability effects. J Pet Sci Eng 39:177–199

Peksa AE, Wolf K-HAA, Zitha PLJ (2015) Bentheimer sandstone revisited for experimental purposes. Mar Pet Geol 67:701e719

Peng S, Hu Q, Dultz S, Zhang M (2012) Using X-ray computed tomography in pore structure characterization for a Berea sandstone: resolution effect. J Hydrol 472–473:254–261

Pentland CH (2010) Measurements of non-wetting phase trapping in porous media. PhD Thesis, Imperial College London

Prodanovic M, Lindquist WB, Seright RS (2006) Porous structure and fluid partitioning in polyethylene cores from 3D X-ray microtomographic imaging. J Colloid Interface Sci 298:282–297

Ramstad T (2018) Bentheimer micro-CT with waterflood. Digital Rocks Portal. http://www.digitalrocksportal.org/projects/172. Accessed 4 February 2021

Ramstad T, Idowu N, Nardi C, Øren P-E (2012) Relative permeability calculations from two-phase flow simulations directly on digital images of porous rocks. Transp Porous Media 94:487–504

Ribeiro CO, de Carvalho Balaban R (2015) Comparative study between Botucatu and Berea sandstone properties. J S Am Earth Sci 62:58–69

Rodríguez de Castro A, Agnaou M, Ahmadi-Sénichault A, Omari A (2019) Application of non-toxic yield stress fluids porosimetry method and pore-network modelling to characterize the pore size distribution of packs of spherical beads. Transp Porous Media 130(3):799–818

Rodríguez de Castro A (2014) Flow experiments of yield stress fluids in porous media as a new porosimetry method. PhD Thesis, Arts et Métiers ParisTech, Paris

Rodríguez de Castro A, Agnaou M, Ahmadi-Sénichault A, Omari A (2020a) Numerical porosimetry: evaluation and comparison of yield stress fluids method, mercury intrusion porosimetry and pore network modelling approaches. Comput Chem Eng 133:106662

Rodríguez de Castro A, Ahmadi-Sénichault A, Omari A (2020b) Determination of the aperture distribution of rough-walled rock fractures with the non-toxic yield stress fluids porosimetry method. Adv Water Resour 146:103794

Rodríguez de Castro A, Ahmadi-Sénichault A, Omari A, Savin S, Madariaga L-F (2016) Characterizing porous media with the yield stress fluids porosimetry method. Transp Porous Media 114(1):213–233

Rodríguez de Castro A, Ahmadi-Sénichault A, Omari A (2018) Using xanthan gum solutions to characterize porous media with the yield stress fluid porosimetry method: robustness of the method and effects of polymer concentration. Transp Porous Media 122(2):357–374

Rodríguez de Castro A, Omari A, Ahmadi-Sénichault A, Bruneau D (2014) Toward a new method of Porosimetry: principles and experiments. Transp Porous Media 101(3):349–364

Rodríguez de Castro A, Goyeau B (2021) A pore network modelling approach to investigate the interplay between local and Darcy viscosities during the flow of shear-thinning fluids in porous media. J Colloid Interface Sci 590:446–457

Rouquerol J, Baron G, Denoyel R, Giesche H, Groen J, Klobes P, Levitz P, Neimark AV, Rigby S, Skudas R, Sing K, Thommes M, Unger K (2012) Liquid intrusion and alternative methods for the

characterization of macroporous materials (IUPAC technical report). Pure Appl Chem 84(1):107–136

Sharqawy MH (2016) Construction of pore network models for Berea and Fontainebleau sandstones using non-linear programing and optimization techniques. Adv Water Resour 98:198–210

Skelland AHP (1967) Non-Newtonian flow and heat transfer. Wiley, New York

Tembely M, AlSumaiti AM, Rahimov K, Jouini MS (2019) Pore-scale modeling of non-Newtonian fluid flow through micro-CT images of rocks. In: Ao SI, Gelman L, Ki H(eds) Transactions on engineering technologies. WCE 2017, Springer, Singapore

Thomson P-R, Aituar-Zhakupova A, Hier-Majumder S (2018) Image segmentation and analysis of pore network geometry in two natural sandstones. Front Earth Sci 6:58

Tsakiroglou CD, Payatakes AC (2000) Characterization of the pore structure of reservoir rocks with the aid of serial sectioning analysis, mercury porosimetry and network simulation. Adv Water Resour 23:773–789

Tsakiroglou CD, Ioannidis MA (2008) Dual-porosity modelling of the pore structure and transport properties of a contaminated soil. Eur J Soil Sci 59:744–761

Tsakiroglou CD, Ioannidis MA, Amirtharaj E, Vizika O (2009) A new approach for the characterization of the pore structure of dual porosity rocks. Chem Eng Sci 64:847–859

Voigt C, Hubálková J, Giesche H, Aneziris CG (2020) Intrusion and extrusion mercury porosimetry measurements at Al2O3-C: influence of measuring parameter. Microporous Mesoporous Mater 299:110125

Wang X, Hou J, Song S, Wang D, Gong L, Ma K, Liu Y, Liu Y, Li Y, Yan L (2018) Combining pressure-controlled porosimetry and rate-controlled porosimetry to investigate the fractal characteristics of full-range pores in tight oil reservoirs. J Pet Sci Eng 171:353–361

Washburn EW (1921) The dynamics of capillary flow. Phys Rev 17:273–283

Wildenschild D, Sheppard AP (2012) X-ray imaging and analysis techniques for quantifying pore-scale structure and processes in subsurface porous medium systems. Adv Water Resour 51:217–246

Xiong Q, Baychev TG, Jivkov AP (2016) Review of pore network modelling of porous media: experimental characterisations, network constructions and applications to reactive transport. J Contam Hydrol 192:101–117